Commun. Comput. Phys.
doi: 10.4208/cicp.081214.250515s

Vol. **18**, No. 4, pp. 901-930
October 2015

A Slope Constrained 4th Order Multi-Moment Finite Volume Method with WENO Limiter

Ziyao Sun[1], Honghui Teng[2] and Feng Xiao[1,*]

[1] *Department of Energy Sciences, Tokyo Institute of Technology, 4259 Nagatsuta, Midori-ku, Yokohama, 226-8502, Japan.*
[2] *State Key Laboratory of High Temperature Gas Dynamics, Institute of Mechanics, Chinese Academy of Sciences, Beijing, 100190, China.*

Received 8 December 2014; Accepted (in revised version) 25 May 2015

Abstract. This paper presents a new and better suited formulation to implement the limiting projection to high-order schemes that make use of high-order local reconstructions for hyperbolic conservation laws. The scheme, so-called MCV-WENO4 (multi-moment Constrained finite Volume with WENO limiter of 4th order) method, is an extension of the MCV method of Ii & Xiao (2009) by adding the 1st order derivative (gradient or slope) at the cell center as an additional constraint for the cell-wise local reconstruction. The gradient is computed from a limiting projection using the WENO (weighted essentially non-oscillatory) reconstruction that is built from the nodal values at 5 solution points within 3 neighboring cells. Different from other existing methods where only the cell-average value is used in the WENO reconstruction, the present method takes account of the solution structure within each mesh cell, and thus minimizes the stencil for reconstruction. The resulting scheme has 4th-order accuracy and is of significant advantage in algorithmic simplicity and computational efficiency. Numerical results of one and two dimensional benchmark tests for scalar and Euler conservation laws are shown to verify the accuracy and oscillation-less property of the scheme.

AMS subject classifications: 65M08, 65M70, 76L05, 76N15

Key words: Multi-moment finite volume method, WENO, flux reconstruction, compressible flow, conservative method, oscillation-suppressing.

1 Introduction

High order numerical methods have got increasingly use in solving fluid dynamic problems for their superior performance in resolving the vortex-dominant flows in comparison with low order methods. Different from the conventional finite volume method

*Corresponding author. *Email addresses:* sun.z.ab@m.titech.ac.jp (Z. Sun), hhteng@imech.ac.cn (H. Teng), xiao@es.titech.ac.jp (F. Xiao)

 ©2015 Global-Science Press

https://doi.org/10.4208/cicp.081214.250515s Published online by Cambridge University Press

(FVM) and finite difference method (FDM), making use of locally (cell-wisely) increased degrees of freedoms (DOFs) to construct high-order schemes is a trend for the past decades in the field of computational fluid dynamics (CFD), which still remains an active research direction. The major advantages of a scheme using high-order local reconstruction (HLR) lie in the spectral-like convergence rate and the adaptivity to unstructured grids. Some representative methods of this sort for CFD applications are the spectral element method [19], the discontinuous Galerkin (DG) method [4–6, 9], the constrained interpolation profile (CIP) method [45, 46], the staggered-grid (SG) Chebyshev multidomain method [16], the spectral volume (SV) method [34, 35], the spectral difference (SD) method [30], multi-moment (constrained) finite volume (MV or MCV) method [3, 13, 14, 43, 44].

Although apparent differences are seen among the aforementioned methods in the details of reconstruction and solution procedures, all of them realize high-order accuracy via locally reconstructed polynomials and guarantee the numerical conservation by introducing an FVM-like constraint condition on the continuity of numerical fluxes across mesh cell boundaries, which are computed through exact or approximate Riemann solvers. From this observation, a general framework for constructing high-order spectral-convergent schemes, so-called Flux Reconstruction (FR) method, was proposed in [12]. The FR formulation treats the point values as the computational variable at the solution points located within each grid cell, which facilitates local reconstructions of high order. An FR scheme computes the point-wise solution via the differential form of the governing equations where the flux function must be reconstructed so as to satisfy the continuity on the cell boundaries. As shown in [12], nearly all existing nodal-value based high order schemes can be interpreted as the subset cases of the FR framework where the correction functions involved in the flux reconstruction procedure makes the difference among the schemes. The FR was extended to unstructured grids under the name of CPR (correction procedure via reconstruction) [36].

We show in the multi-moment constrained flux reconstruction (MMC-FR) method [38] that the flux function can be reconstructed more flexibly with a wider variety of constraint conditions. We demonstrated that stable and more efficient schemes can be devised by making use of not only the point values but also the derivatives of different orders at different constraint points. The class of MCV schemes [14] can be devised straightforwardly from various constraint conditions under the MMC-FR framework.

Despite the superiority of the schemes with HLR in resolving complex structures of smoothness, numerical oscillations associated with discontinuities turns out to be another problem. Using some special interpolation function, such as the rational function in [39, 40, 42], proves to be effective in suppressing numerical oscillations. Being a more general approach, nonlinear limiting projection can be used to prevent the spurious oscillations in the presence of discontinuities or large jumps. For example, total variation bounded (TVB) limiters were used in the DG method [4–6] and other HLR methods mentioned before, and proved to be effective in computing even shock-dominant flows. Compared to the TVB limiter, the weighted essentially non-oscillatory (WENO) limiter [15, 18] is more attractive because it is able to effectively suppress the numerical oscillation in

https://doi.org/10.4208/cicp.081214.250515s Published online by Cambridge University Press

the vicinity of discontinuity and retain the highest possible accuracy in smooth region through an automatic weighting switch. The WENO limiter was designed originally for finite volume and finite difference methods [26] and implemented to the DG method in [21], where the fifth order WENO scheme of finite volume type was constructed by using the cell average values over a wide stencil. The WENO reconstruction is then used to project the point values (PVs) at the Gauss quadrature points in the target cell. This formulation only uses the cell averages even though more information (DOFs) are available in the HLR of DG. An effort was made by the same authors to use more local information from the cell-wise high-order polynomial by devising a Hermite-type WENO limiter [20], which uses the derivatives as another moment in the reconstruction and looks better suited for the HLR used in DG, and thus makes the stencil more compact. Among other successive works, a more general formulation that maps different moments to cell average or point value for making use of the conventional WENO reconstruction is developed in [11]. A simple WENO limiter has been recently proposed in [48] for DG and applied to FR/CPR in [7]. This scheme minimizes the stencil for WENO reconstruction and only uses the target cell and its immediate neighbors.

In this paper, we present a new formulation to incorporate the WENO limiter to an MCV scheme as a practice toward the well-matched implementation of WENO to HLR schemes. The proposed scheme, MCV-WENO4 (Multi-moment Constrained finite Volume with WENO limiter of 4th order) method, is based on the three-point MCV scheme [14] and introduces a slope constraint computed from a WENO reconstruction that uses the nodal values within three adjacent mesh elements. Excellent numerical results were obtained for the benchmark tests.

This paper is organized as follows. The three-point MCV scheme with slope constraint is introduced under the MMC-FR framework in Section 2. A 4th order WENO limiter that uses the nodal values at 5 points in the target cell and its immediate neighbors is presented in Section 3. Section 4 shows the numerical results of the widely used benchmark tests in one and two dimensions to verify the proposed scheme, and a brief summary ends the paper in Section 5.

2 MMC-FR formulation and 3-point MCV scheme with slope constraint

Being an extension of the FR formulation of Huynh [12], the MMC-FR [38] is briefed at first for completeness in this section. A new scheme is then devised under the MMC-FR framework by adding a slope constraint to the 3-point MCV scheme.

2.1 Brief of the MMC-FR formulation

We consider the following hyperbolic conservation law

https://doi.org/10.4208/cicp.081214.250515s Published online by Cambridge University Press

$$\frac{\partial u}{\partial t}+\frac{\partial f}{\partial x}=0, \tag{2.1}$$

where u is the solution function, and $f(u)$ the flux function.

The computational domain is divided into I non-overlapping cells or elements $\Omega_i=[x_{i-\frac{1}{2}},x_{i+\frac{1}{2}}]$, $i=1,2,\cdots,I$, and K solution points x_{ik}, $k=1,2,\cdots,K$, are set over Ω_i where the solution u_{ik}, $k=1,2,\cdots,K$, is computed. As shown in the FR formulation of Huynh [12], given a properly approximated numerical flux function $\hat{f}_i(x)$, we can update the solutions within Ω_i by the following point-wise semi-discretised equations at solution points x_{ik},

$$\frac{du_{ik}}{dt}=-\left(\frac{d\hat{f}_i(x)}{dx}\right)_{ik}, \quad k=1,2,\cdots,K. \tag{2.2}$$

The above equation (2.2) is of differential form, which covers a wide range of schemes including the collocation method, spectral element method and nodal DG method. The central task left now is how to reconstruct the flux function $\hat{f}_i(x)$. In principle, the way to reconstruct $\hat{f}_i(x)$ makes difference among the numerical schemes.

Given the solution u_{ik} at x_{ik}, $k=1,2,\cdots,K$, a piece-wise Lagrange interpolation polynomial of degree $K-1$ for Ω_i reads

$$\tilde{u}_i(x)=\sum_{k=1}^{K}u_{ik}\phi_{ik}(x), \tag{2.3}$$

where $\phi_{ik}(x)$ is the Lagrange basis function,

$$\phi_{ik}(x)=\prod_{l=1,l\neq k}^{K}\frac{x-x_{il}}{x_{ik}-x_{il}}. \tag{2.4}$$

Given flux $f(u)$ as the function of solution u, we have the flux function f_{ik} at the solution points x_{ik}, $k=1,2,\cdots,K$, simply by $f_{ik}=f(u_{ik})$. The piece-wisely reconstructed polynomial for flux function is then obtained as

$$\tilde{f}_i(x)=\sum_{k=1}^{K}f_{ik}\phi_{ik}(x), \tag{2.5}$$

which is of degree $K-1$, same as that for the solution function $u_i(x)$.

We call (2.5) the primary reconstruction which is separately constructed over each cell and thus broken from cell by cell. As shown later, the primary reconstruction is not limited to (2.4) or (2.5). Other conditions might be also added so that the resulting scheme have some desired numerical properties. In general, the primary reconstruction cannot be directly used to calculate (2.2). Further modification is required to ensure that the modified numerical flux function $\hat{f}_i(x)$ is at least C^0 continuous at the two ends $x_{i-\frac{1}{2}}$

https://doi.org/10.4208/cicp.081214.250515s Published online by Cambridge University Press

and $x_{i+\frac{1}{2}}$ of cell Ω_i, which is the necessary condition for numerical conservation and computational stability.

In [38], we demonstrate that the modified flux function, $\hat{f}_i(x)$, can be reconstructed more flexibly with a wider variety of constraint conditions in a more straightforward and intuitive way. The resulting formulation is called multi-moment constrained flux reconstruction (MMC-FR), which provides a platform to devise new schemes. The numerical procedure of MMC-FR to construct the modified flux function $\hat{f}_i(x)$ is summarized as follows.

1. Compute the primary reconstruction for the solution u or flux function $f(u)$ through (2.3) or (2.5) for all cell Ω_i, $i=1,2,\cdots,I$.

2. Compute the solution or flux function on the two sides of the cell boundary $x_{i-\frac{1}{2}}$, for example, by $f^L_{i-\frac{1}{2}}=\tilde{f}_{i-1}(x_{i-\frac{1}{2}})$ and $f^R_{i-\frac{1}{2}}=\tilde{f}_i(x_{i-\frac{1}{2}})$, as well as their derivatives $f^{[m]L}_{xi-\frac{1}{2}}=\tilde{f}^{[m]}_{xi-1}(x_{i-\frac{1}{2}})=\frac{d^m}{dx^m}\left(\tilde{f}_{i-1}(x_{i-\frac{1}{2}})\right)$ and $f^{[m]R}_{xi-\frac{1}{2}}=\tilde{f}^{[m]}_{xi}(x_{i-\frac{1}{2}})=\frac{d^m}{dx^m}\left(\tilde{f}_i(x_{i-\frac{1}{2}})\right)$ in case they are not continuous and to be used as the constraint conditions;

3. Find the flux function, $f^{\mathcal{B}}_{i-\frac{1}{2}}$, and its derivatives, $f^{[m]\mathcal{B}}_{xi-\frac{1}{2}}$, at the cell boundary by solving

$$\begin{aligned} f^{\mathcal{B}}_{i-\frac{1}{2}} &= \text{Riemann}\left(f^L_{i-\frac{1}{2}}, f^R_{i-\frac{1}{2}}\right), \\ f^{[m]\mathcal{B}}_{xi-\frac{1}{2}} &= \text{DRiemann}\left(f^{[m]L}_{xi-\frac{1}{2}}, f^{[m]R}_{xi-\frac{1}{2}}\right), \end{aligned} \tag{2.6}$$

   where "Riemann$(\cdot\,,\cdot)$" and "DRiemann$(\cdot\,,\cdot)$" denote the solvers for the Godunov and derivative Riemann problems.

4. The modified flux function $\hat{f}_i(x)$ of degree K' ($K'\geq K$) is then constructed by properly choosing $K'+1$ constraints including the continuity conditions of flux function, as well as its derivatives if needed, at the cell boundaries. Other constraint conditions can be chosen as the point values or derivatives directly computed from the primary flux function $\tilde{f}_i(x)$ at the constraint points inside the mesh cell.

5. Given the modified flux function $\hat{f}_i(x)$, the numerical solutions are updated by solving the semi-discretised equations (2.2) through time integration.

It is noted that there are options for a user to choose for which variable the primary reconstruction is made, such as the conservative variable, the flux function or the characteristic variable in the system equations.

In the MMC-FR formulation, we need to compute the derivatives of the flux function at cell boundaries which are usually discontinuous and need to be evaluated from the primary reconstructions of the neighboring cells. It is generally known as the derivative Riemann problems. The high-order linear and homogeneous derivative Riemann

https://doi.org/10.4208/cicp.081214.250515s Published online by Cambridge University Press

problems are detailed in [31, 33] for the hyperbolic systems. As addressed in [33], since the first-instant plays a leading role in the interaction of the two states, the derivative Riemann problems with the linearization simplifications provide a reasonable accuracy.

The extension of MMC-FR method to two dimensional case on a structured mesh is straightforward through the tensor product of 1D algorithm. We consider the conservation law of (2.7) in two dimensions,

$$\begin{cases} u_t+f(u)_x+g(u)_y=0, \\ u(x,y,0)=u_0(x,y), \end{cases} \tag{2.7}$$

where $f(u)$ is the flux function in x direction and $g(u)$ in y direction respectively. The flux reconstruction is conducted over each line segment, e.g. for target cell ij, in x direction, we construct the flux function along line segments $\overline{x_{i-\frac{1}{2}}x_{i+\frac{1}{2}}}\bigcap y_{jk}$, $k=1,2,\cdots,K$, while for y direction the flux function can be obtained by the reconstructions over line segments $\overline{y_{j-\frac{1}{2}}y_{j+\frac{1}{2}}}\bigcap x_{ik}$, $k=1,2,\cdots,K$. The solution points are updated from the summation of the spatial derivatives of flux functions for x and y directions.

2.2 3-point MCV scheme with slope constraint

We describe the 3-point MCV scheme with slope constraint, referred to as MCV-SC hereafter, as an example of the MMC-FR method. Three solution points x_{ik}, $k=1,2,3$, are used over each cell Ω_i. In the present scheme we locate the solution points respectively at $x_{i1}=x_{i-\frac{1}{2}}$, $x_{i2}=x_i=(x_{i-\frac{1}{2}}+x_{i+\frac{1}{2}})/2$ and $x_{i3}=x_{i+\frac{1}{2}}$. The solutions u_{ik}, $k=1,2,3$, can be updated through the semi-discretized equation (2.2).

It should be noted that because $x_{i1}=x_{i-\frac{1}{2}}$ and $x_{i3}=x_{i+\frac{1}{2}}$ are the two ends of the cell and u_{i1} is shared by cells Ω_{i-1} and Ω_i, i.e. $u_{(i-1)3}=u_{i1}=u_{i-\frac{1}{2}}$, only two of (2.2) need to be computed.

Given the solutions u_{ik}, $k=1,2,3$, the primary reconstruction is a quadratic Lagrange interpolation built to approximate the flux function, which results in the MCV3 (Multi-moment constrained finite volume method of 3rd order) scheme as shown in [14, 38]. Following the basic idea in [41], we add another constraint condition as the first-order derivative (slope), $f_x^{[1]}(x_i)$, at the cell center and build the primary flux reconstruction as a cubic polynomial $\tilde{f}_i(x)$ from the following conditions,

$$\begin{cases} \tilde{f}_i(x_{i-\frac{1}{2}})=f(u_{i1}); \\ \tilde{f}_i(x_i)=f(u_{i2}); \\ \tilde{f}_i(x_{i+\frac{1}{2}})=f(u_{i3}); \\ \tilde{f}_{xi}^{[1]}(x_i)=f_x^{[1]}(x_i). \end{cases} \tag{2.8}$$

Here the first-order derivative $f_x^{[1]}(x_i)$ is obtained from an interpolation that may involve

https://doi.org/10.4208/cicp.081214.250515s Published online by Cambridge University Press

cell Ω_i and its immediate neighbors. For example, a fourth-order approximation is obtained by using the nodal values $f(u_{i\pm\frac{1}{2}})$ and $f(u_{i\pm1})$ from two neighboring cells,

$$f_x^{[1]}(x_i)=\frac{8f(u_{i+\frac{1}{2}})-8f(u_{i-\frac{1}{2}})+f(u_{i-1})-f(u_{i+1})}{6\Delta x_i}. \tag{2.9}$$

Using $f_x^{[1]}(x_i)$ as a constraint condition, we can make the scheme to have the desired numerical properties. A 4th-order scheme can be constructed if approximation (2.9) is used in (2.8). We refer it as the MCV-SC4 (MCV-SC of 4th order) in this paper.

As mentioned before, interpolation $\tilde{f}_i(x)$ cannot be immediately used in (2.2) to update the nodal solutions, but is used to find the left and right-side derivative values of the flux function at the cell boundaries. It is observed from (2.8) that the primary reconstruction $\tilde{f}(x)$ is continuous at the cell boundary, i.e. $\tilde{f}_{i-1}(x_{i-\frac{1}{2}})=\tilde{f}_i(x_{i-\frac{1}{2}})=f(u_{i-\frac{1}{2}})$.

In the present scheme, we impose the following constraint conditions to the modified flux reconstruction $\hat{f}_i(x)$ in terms of both flux function and its first-order derivative, same as the MCV3 scheme shown in [38],

$$\begin{cases}\hat{f}_i(x_{i\pm\frac{1}{2}})=f_i(u_{i\pm\frac{1}{2}}),\\ \hat{f}_{xi}^{[1]}(x_{i\pm\frac{1}{2}})=f_x^{[1]B}(x_{i\pm\frac{1}{2}}),\end{cases} \tag{2.10}$$

where $f_i(u_{i\pm\frac{1}{2}})$ can be calculated directly with $u_{i\pm\frac{1}{2}}$ updated every time step, and $f_x^{[1]B}(x_{i\pm\frac{1}{2}})$ are the approximations of the first-order derivatives of the flux function at cell boundaries, which need to be computed as the solutions of the Derivative Riemann problems based on the left and right-side values at the cell boundaries as discussed before.

Constraint condition (2.10) yields a Hermite interpolation to determine the modified flux function which is written in a cubic polynomial as,

$$\begin{cases}\hat{f}_i(x)=\left(2\left(f_i(u_{i-\frac{1}{2}})-f_i(u_{i+\frac{1}{2}})\right)+\Delta x_i\left(f_x^{[1]B}(x_{i-\frac{1}{2}})+f_x^{[1]B}(x_{i+\frac{1}{2}})\right)\right)\xi^3\\ \qquad\quad+\left(3\left(f_i(u_{i+\frac{1}{2}})-f_i(u_{i-\frac{1}{2}})\right)-\Delta x_i\left(2f_x^{[1]B}(x_{i-\frac{1}{2}})+f_x^{[1]B}(x_{i+\frac{1}{2}})\right)\right)\xi^2\\ \qquad\quad+\Delta x_i f_x^{[1]B}(x_{i-\frac{1}{2}})\xi+f_i(u_{i-\frac{1}{2}}),\end{cases} \tag{2.11}$$

where $\xi=(x-x_{i-\frac{1}{2}})/\Delta x_i$.

The derivatives of the modified flux function at the solution points are obtained as

$$\begin{cases}\left(\dfrac{d\hat{f}_i(x)}{dx}\right)_{i1}=f_x^{[1]B}(x_{i-\frac{1}{2}});\\ \left(\dfrac{d\hat{f}_i(x)}{dx}\right)_{i2}=\dfrac{3}{2\Delta x_i}\left(f_i(u_{i+\frac{1}{2}})-f_i(u_{i-\frac{1}{2}})\right)-\dfrac{1}{4}\left(f_x^{[1]B}(x_{i-\frac{1}{2}})+f_x^{[1]B}(x_{i+\frac{1}{2}})\right);\\ \left(\dfrac{d\hat{f}_i(x)}{dx}\right)_{i3}=f_x^{[1]B}(x_{i+\frac{1}{2}}).\end{cases} \tag{2.12}$$

https://doi.org/10.4208/cicp.081214.250515s Published online by Cambridge University Press

The solutions are then immediately computed by (2.2) with a proper time integration algorithm. We note here again that the boundary values u_{i1} and u_{i3} are shared by the two neighboring cells, and only following two semi-discretized equations need to be solved for each cell,

$$\begin{cases} \dfrac{du_{i1}}{dt} = f_x^{[1]B}(x_{i-\frac{1}{2}}); \\ \dfrac{du_{i2}}{dt} = \dfrac{3}{2\Delta x_i}\left(f_i(u_{i+\frac{1}{2}}) - f_i(u_{i-\frac{1}{2}})\right) - \dfrac{1}{4}\left(f_x^{[1]B}(x_{i-\frac{1}{2}}) + f_x^{[1]B}(x_{i+\frac{1}{2}})\right). \end{cases} \tag{2.13}$$

As discussed in [2,17], the MCV method is more computationally efficient in comparison with DG as well as other HLR based schemes regarding both memory requirement and CPU cost.

3 WENO limiter

In this section, we present the details of the new WENO limiter for 3-point MCV scheme. The resulting scheme is called MCV-WENO4 (Multi-moment Constrained finite Volume with WENO limiter of 4th order) method. The basic idea of this WENO limiter is to reconstruct the 1st order derivative at the cell center for the MCV-SC scheme described above. The WENO reconstructed 1st order derivative is used in (2.8) to construct the primary flux reconstruction locally within each cell. Then, the modified flux reconstruction procedure of MCV-SC scheme is applied without any change. It is noted that the present scheme has much less dissipation error to the smooth solution. Unlike other existing WENO limiters for the DG method, the present WENO projection applies to all cells not just limited to the so-called "trouble cells" which is identified by the TVB criterion and involves artificial parameter. Shown in the numerical results, the smooth solutions are accurately reproduced without significant numerical dissipation.

3.1 WENO reconstruction for first-order derivative: Scalar case

We describe the WENO reconstruction of conservative variable $u(x)$ for cell Ω_i. For MCV-WENO4 scheme, we have three small stencils $S_j = \left\{x_{i-1+\frac{j}{2}}, x_{i-\frac{1}{2}+\frac{j}{2}}, x_{i+\frac{j}{2}}\right\}$, $j=0,1,2$, and one large stencil $S_3 = \left\{x_{i-1}, x_{i-\frac{1}{2}}, x_i, x_{i+\frac{1}{2}}, x_{i+1}\right\}$. The distribution of the stencil is shown in Fig. 1. Then, we can construct a 2nd-degree polynomial through the interpolation of three PVs inside each small stencil. Here the polynomial is denoted by $q_j(x)$ associated with each of the stencils S_j, $j=0,1,2$. The 1st order spatial derivative at the center of cell Ω_i can be approximated with second order accuracy respectively from the derivative of

https://doi.org/10.4208/cicp.081214.250515s Published online by Cambridge University Press

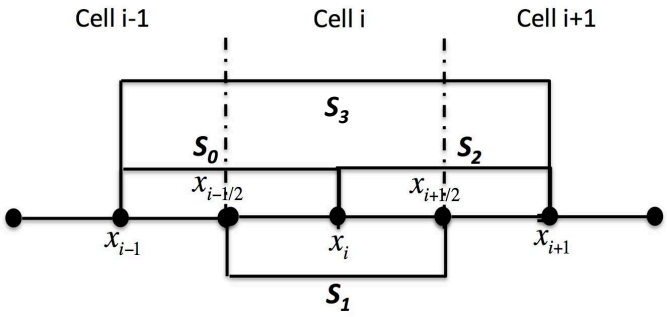


Fig. 1: Reconstruction stencils for the new WENO limiter.

the reconstructed polynomial in each stencil as

$$\begin{aligned} q_{x0}^{[1]}(x_i) &= \frac{3u_i+u_{i-1}-4u_{i-\frac{1}{2}}}{\Delta x_i}, \\ q_{x1}^{[1]}(x_i) &= \frac{u_{i+\frac{1}{2}}-u_{i-\frac{1}{2}}}{\Delta x_i}, \\ q_{x2}^{[1]}(x_i) &= -\frac{3u_i+u_{i+1}-4u_{i+\frac{1}{2}}}{\Delta x_i}. \end{aligned} \tag{3.1}$$

Meanwhile, we have a fourth-degree polynomial reconstruction denoted by $Q_i(x)$ in stencil S_3 which has the first-order derivative at cell center as

$$Q_{xi}^{[1]}(x_i) = \frac{8u_{i+\frac{1}{2}}+u_{i-1}-8u_{i-\frac{1}{2}}-u_{i+1}}{6\Delta x_i}. \tag{3.2}$$

Given (3.2), we can re-write the 1st order derivative at the cell center with $4th$ order accuracy by the linear combination of the three 2nd order approximations, i.e.

$$Q_x^{[1]}(x_i) = \sum_{j=0}^{2} \gamma_j q_{xj}^{[1]}(x_i), \tag{3.3}$$

where

$$\gamma_0 = \frac{1}{6}, \quad \gamma_1 = \frac{2}{3}, \quad \gamma_2 = \frac{1}{6}. \tag{3.4}$$

Following the spirit of existing WENO schemes, instead of (3.4) nonlinear weighting can be designed to effectively suppress spurious oscillation near discontinuity and maintain numerical accuracy in smooth region.

We define the smoothness indicator by

$$\beta_j = \sum_{l=1}^{2} \int_{x_{i-\frac{1}{8}}}^{x_{i+\frac{1}{8}}} \Delta x_i^{2l-1} \left(\frac{\partial^l q_j(x)}{\partial x^l} \right)^2 dx, \quad j=0,1,2; \tag{3.5}$$

https://doi.org/10.4208/cicp.081214.250515s Published online by Cambridge University Press

which measures the smoothness of the polynomial function in the target area. Compared with the smoothness indicator of the conventional WENO scheme, we modify the upper and lower limits of integral from $x_{i-\frac{1}{2}}$ and $x_{i+\frac{1}{2}}$ to $x_{i-\frac{1}{8}}$ and $x_{i+\frac{1}{8}}$ in order to match the compact WENO reconstruction stencil used in the present scheme.

Regarding the WENO reconstruction, some successive works have been conducted to improve the accuracy of the classic WENO [15] by using different nonlinear weights and smoothness measurements in the WENO reconstruction, such as the WENO-M [8] and WENO-Z [1] schemes. Shen and Zha [23, 24] provided a detail analysis how these scheme behave over a transition cell where smooth region and discontinuity connect, and proposed an optimal estimation of the first-order derivative for the transition cell. In the present paper, we adopt the scheme in [23] and calculate the nonlinear weights ω_j, $j=0,1,2$, as the functions of β_j and γ_j by

$$\{\omega_0,\omega_1,\omega_2\}=\begin{cases}\left\{\frac{1}{3},\frac{2}{3},0\right\} & \text{if } \tau_4^0\le\min(\beta_j) \text{ and } \tau_4^1>\min(\beta_j),\\ \left\{0,\frac{2}{3},\frac{1}{3}\right\} & \text{if } \tau_4^0>\min(\beta_j) \text{ and } \tau_4^1\le\min(\beta_j),\\ \left\{\omega_0^Z,\omega_1^Z,\omega_2^Z\right\} & \text{otherwise;}\end{cases} \tag{3.6}$$

where

$$\tau_4^0=|\beta_0-\beta_1|,\quad \tau_4^1=|\beta_1-\beta_2|, \tag{3.7}$$

and $\{\omega_0^Z,\omega_1^Z,\omega_2^Z\}$ are the nonlinear weights obtained from the WENO-Z scheme [1], which are given by

$$\omega_j^Z=\frac{\alpha_j^Z}{\sum_{k=0}^2\alpha_k^Z},\quad \alpha_j^Z=\gamma_j\left(1+\frac{\tau_5}{\beta_j+\epsilon}\right),\quad j=0,1,2, \tag{3.8}$$

where ϵ is equal to 10^{-40} and $\tau_5=|\beta_2-\beta_0|$.

It is noted that our numerical experiments don't show noticeable difference between (3.6) and the WENO-Z scheme.

Finally, we can get the WENO reconstructed first order derivative $\tilde{Q}_x^{[1]}(x_i)$ by

$$\tilde{Q}_x^{[1]}(x_i)=\sum_{j=0}^{2}\omega_j q_{xj}^{[1]}(x_i). \tag{3.9}$$

We assume that the WENO reconstruction is conducted for the conservative variable, and summarize the MCV-WENO4 method as followings:

1. Get the 1st order derivative at the center of the target cell, $q_{xj}^{[1]}(x_i)$, $j=0,1,2$, by (3.1) for each small stencil;
2. Calculate the smoothness indicator for each stencil by (3.5);

https://doi.org/10.4208/cicp.081214.250515s Published online by Cambridge University Press

3. Obtain the nonlinear weights for each stencil using (3.6);
4. Compute the modified 1st order derivative at cell center by (3.9);
5. Replace the 1st order derivative at cell center $f_x^{[1]}(x_i)$ in (2.8) by that computed from the WENO reconstruction;
6. Get the primary reconstruction from the constraint conditions (2.8);
7. Repeat the rest steps of the MCV-SC scheme.

For multi-dimensional structured grids which can be mapped to a Cartesian grid, the WENO reconstruction is carried out along the line segment in each direction separately with the 1D algorithm given above.

3.2 WENO reconstruction for first-order derivative: Euler equations

The 1D Euler equations for ideal gas are given by

$$\mathbf{U}_t+\mathbf{F}(\mathbf{U})_x=0, \tag{3.10}$$

where

$$\mathbf{U}=\begin{pmatrix}u^{(1)}\\u^{(2)}\\u^{(3)}\end{pmatrix}=\begin{pmatrix}\rho\\\rho v\\E\end{pmatrix},\quad \mathbf{F}(\mathbf{U})=\begin{pmatrix}f^{(1)}\\f^{(2)}\\f^{(3)}\end{pmatrix}=\begin{pmatrix}\rho v\\\rho v^2+p\\v(E+p)\end{pmatrix}. \tag{3.11}$$

Here ρ is density, v velocity, p pressure and E total energy. We use the equation of state (EOS) of ideal gas, i.e.

$$E=\frac{p}{\gamma-1}+\frac{1}{2}\rho v^2, \tag{3.12}$$

where $\gamma=1.4$. The Jacobian matrix of the flux function is defined by $\mathbf{A}=\partial\mathbf{F}/\partial\mathbf{U}$.

For the Euler system, the WENO reconstruction is carried out in terms of the characteristic variables. To this end, the vector of conservative variables is mapped firstly to the characteristic variables $\mathbf{W}=(w^{(1)},w^{(2)},w^{(3)})^T$ using the left eigenvectors of the Jacobian matrix $\overline{\mathbf{A}}_{i+\frac{1}{2}}$ computed from Roe averaging,

$$\mathbf{W}_j=\overline{\mathbf{R}}_{i+\frac{1}{2}}^{-1}\mathbf{U}_j,\quad j=i-1,\ i-\frac{1}{2},\ i,\ i+\frac{1}{2},\ i+1, \tag{3.13}$$

where $\overline{\mathbf{R}}_{i+\frac{1}{2}}^{-1}$ is a 3×3 matrix whose rows are the left eigenvectors of Jacobian matrix $\overline{\mathbf{A}}_{i+\frac{1}{2}}$. Then, all the WENO reconstruction is conducted for the characteristic variables $\mathbf{W}_j$ to get the 1st order derivative of characteristic variables, $\mathbf{W}_{xi}^{[1]}$, at the cell center. After that, we project the derivative of characteristic variable back to the conservative variables by

$$\mathbf{U}_{xi}^{[1]}=\overline{\mathbf{R}}_{i+\frac{1}{2}}\mathbf{W}_{xi}^{[1]}, \tag{3.14}$$

https://doi.org/10.4208/cicp.081214.250515s Published online by Cambridge University Press

where $\overline{\mathbf{R}}_{i+\frac{1}{2}}$ is a 3×3 matrix of which the columns are the right eigenvectors of Jacobian matrix $\overline{\mathbf{A}}_{i+\frac{1}{2}}$. After obtaining $\mathbf{U}^{[1]}_{xi}$, we make the primary reconstruction $\tilde{\mathbf{U}}_i(x)$ from the constraints (2.8) component-wisely for each conservative variable. Then, the 1st order derivative at cell boundary $x_{i+\frac{1}{2}}$ can be obtained from the reconstructed solution function by $\mathbf{U}^{[1]L}_{xi+\frac{1}{2}}=\frac{d}{dx}\tilde{\mathbf{U}}_i(x_{i+\frac{1}{2}})$. The derivative of the corresponding flux function is then computed by

$$\mathbf{F}^{[1]L}_{xi+\frac{1}{2}}=\overline{\mathbf{A}}_{i+\frac{1}{2}}\mathbf{U}^{[1]L}_{xi+\frac{1}{2}}. \tag{3.15}$$

It is noted that we use the Roe-averaged Jacobian matrix at the right boundary $x_{i+\frac{1}{2}}$ of cell Ω_i in the characteristic field decomposition. In this case, the WENO modified first order derivative at the cell center is used to compute the 1st order derivative at the right boundary $x_{i+\frac{1}{2}}$. When calculating the 1st order derivative at the left boundary $x_{i-\frac{1}{2}}$, we use the Roe-averaged Jacobian matrix, $\overline{\mathbf{A}}_{i-\frac{1}{2}}$, at the left boundary, which results in $\mathbf{U}^{[1]R}_{xi-\frac{1}{2}}=\frac{d}{dx}\tilde{\mathbf{U}}_i(x_{i-\frac{1}{2}})$ and

$$\mathbf{F}^{[1]R}_{xi-\frac{1}{2}}=\overline{\mathbf{A}}_{i-\frac{1}{2}}\mathbf{U}^{[1]R}_{xi-\frac{1}{2}}. \tag{3.16}$$

Having obtained the left and right values of the derivatives of the conservative variables and flux functions at cell boundaries, the numerical approximation of the flux derivative is computed by the Roe approximate Riemann solver [22], i.e.

$$\mathbf{F}^{[1]B}_{xi+\frac{1}{2}}=\frac{1}{2}\left(\mathbf{F}^{[1]L}_{xi+\frac{1}{2}}+\mathbf{F}^{[1]R}_{xi+\frac{1}{2}}-\overline{\mathbf{A}}_{i+\frac{1}{2}}\left(\mathbf{U}^{[1]R}_{xi+\frac{1}{2}}-\mathbf{U}^{[1]L}_{xi+\frac{1}{2}}\right)\right). \tag{3.17}$$

We have so far described the spatial discretization and obtained the semi-discretized ordinary differential equations (ODEs) with respect to time. In the numerical tests presented in this paper, we use the five stage fourth order SSP Runge-Kutta method (SSPRK(5,4)) developed by Spiteri and Ruuth [29].

4 Numerical experiments

In this section, we give the numerical results for some widely used benchmark tests to illustrate the performance of the MCV-WENO4 method presented in this paper. The largest allowable CFL number for MCV-WENO4 scheme with the SSP Runge-Kutta method (SSPRK(5,4)) is 0.6. Here we use CFL$=0.4$ in all numerical tests presented in this paper.

4.1 1D linear advection equation

In this subsection, the numerical tests to advect the 1D profile are computed by the MCV-WENO4 method with the linear advection equation defined by

$$u_t+u_x=0. \tag{4.1}$$

https://doi.org/10.4208/cicp.081214.250515s Published online by Cambridge University Press

Example 4.1 (Accuracy test)**.** For this test, we use the grid refinement to check the convergence rate of our scheme. The initial smooth distribution is given as

$$u(x,0)=\sin(\pi x),\quad x\in[-1,1]. \tag{4.2}$$

The grid is refined by doubling the grid number for the computational domain, and the L_1 errors and L_∞ errors at $t=2.0$ (after one period) are calculated with different grid resolutions. We show the numerical errors and the convergence rate for MCV-WENO4 scheme as well as MCV-SC4 scheme in Table 1. We can see that our scheme uniformly converges to 4th order accuracy. We also notice that the new WENO limiter can maintain not only the convergence rate but also the magnitude of the errors of the original MCV-SC4 scheme.

Table 1: Numerical errors and convergence rate for 1D advection equation, $t=2.0$.

N	MCV-SC4 scheme				MCV-WENO4 scheme			
	L_1 error	Order	L_∞	Order	L_1 error	Order	L_∞	Order
10	7.45e-04		1.15e-03		7.60e-04		1.31e-03	
20	4.94e-05	3.91	7.65e-05	3.91	4.95e-05	4.05	7.72e-05	4.08
40	3.12e-06	3.99	4.88e-06	3.97	3.12e-06	3.98	4.88e-06	3.98
80	1.96e-07	3.99	3.07e-07	3.99	1.96e-07	3.99	3.07e-07	3.99
160	1.23e-08	4.00	1.92e-08	4.00	1.23e-08	4.00	1.92e-08	4.00
320	7.67e-10	4.00	1.20e-09	4.00	7.67e-10	4.00	1.20e-09	4.00

Example 4.2 (Advection of a square wave)**.** This test is used to verify the ability of the MCV-WENO4 scheme to capture the jump discontinuities. The initial profile is set as

$$u(x,0)=\begin{cases}1, & \text{when } |x|\leqslant 0.4,\\ 0, & \text{otherwise.}\end{cases} \tag{4.3}$$

In Fig. 2, we show the numerical solution by the open squares which is computed by the MCV-WENO4 scheme with 200 cells over $[-1,1]$ at $t=2.0$ (after one period). We can clearly see that after one period, the numerical solution doesn't cause spurious oscillations in the vicinity of the jump discontinuities located at $x=0.4$ and $x=-0.4$.

Example 4.3 (Jiang and Shu's test)**.** This test was proposed in [15]. Here we use it to evaluate the ability of the MCV-WENO4 scheme in resolving both discontinuities and smooth solutions. The initial profile is set by

$$u(x,0)=\begin{cases}\frac{1}{6}(G(x,\beta,z-\delta)+G(x,\beta,z+\delta)+4G(x,\beta,z)), & -0.8\leqslant x\leqslant -0.6,\\ 1, & -0.4\leqslant x\leqslant -0.2,\\ 1-|10(x-0.1)|, & 0.0\leqslant x\leqslant 0.2,\\ \frac{1}{6}(F(x,\alpha,a-\delta)+F(x,\alpha,a+\delta)+4F(x,\alpha,a)), & 0.4\leqslant x\leqslant 0.6,\\ 0, & \text{otherwise,}\end{cases} \tag{4.4}$$

https://doi.org/10.4208/cicp.081214.250515s Published online by Cambridge University Press

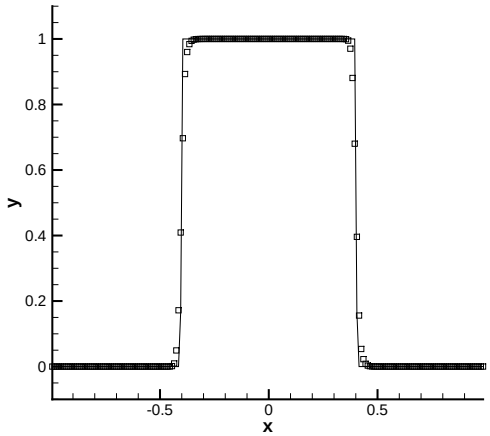


Fig. 2: Advection of a square wave after one period ($t=2.0$) with 200 grid cells. The solid line indicates the exact solution and the open squares the numerical solution.

where the computation domain is $[-1,1]$. The function F and G is defined by

$$G(x,\beta,z)=\exp\left(-\beta(x-z)^2\right),\quad F(x,\alpha,a)=\sqrt{\max(1-\alpha^2(x-a)^2,0)}, \tag{4.5}$$

and the coefficients to determine the initial profile are given by

$$a=0.5,\quad z=0.7,\quad \delta=0.005,\quad \alpha=10.0,\quad \beta=\log 2/(36\delta^2). \tag{4.6}$$

The numerical solution computed over a 200-cell mesh after one period ($t=2.0$) is shown in Fig. 3. Here we use the periodic boundary condition. The numerical results show that the MCV-WENO4 scheme can effectively suppress the oscillations near the discontinuities while keeping the high order accuracy for a smooth profile.

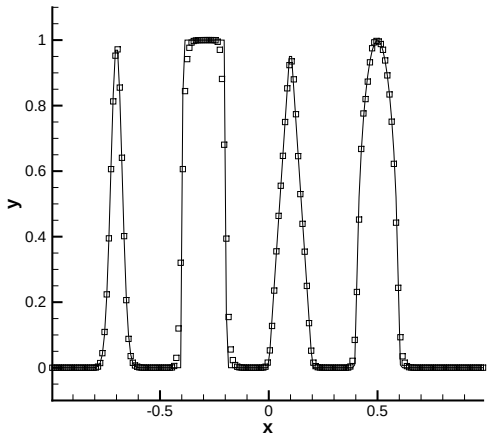


Fig. 3: Numerical results of Jiang and Shu's linear advection test at $t=2.0$ with 200 grid cells.

https://doi.org/10.4208/cicp.081214.250515s Published online by Cambridge University Press

4.2 1D inviscid Burgers' equation

In this subsection, we consider the 1D inviscid Burgers' equation

$$u_t+\left(\frac{u^2}{2}\right)_x=0. \tag{4.7}$$

In the examples of the 1D inviscid Burgers equation presented in this paper, the derivative Riemann problem is computed by a pure upwinding scheme at the cell boundary $x_{i+\frac{1}{2}}$ as

$$f^{[1]}_{xi+\frac{1}{2}}=\frac{1}{2}\left(f^{[1]L}_{xi+\frac{1}{2}}+f^{[1]R}_{xi+\frac{1}{2}}-\mathrm{sgn}(\alpha_{i+\frac{1}{2}})(f^{[1]L}_{xi+\frac{1}{2}}+f^{[1]R}_{xi+\frac{1}{2}})\right), \tag{4.8}$$

where $\alpha_{i+\frac{1}{2}}=\frac{\bar{u}_i+\bar{u}_{i+1}}{2}$, and $\bar{u}_i$ is the integrated average value for cell Ω_i. The WENO interpolation is performed in terms of the flux function $f(u)=\frac{u^2}{2}$.

Example 4.4 (Accuracy test)**.** This test starts with a smooth initial condition, $u(x,0)=0.5+\sin(\pi x)$. The exact solution remains smooth up to $T=1.0/\pi$, and then a moving shock and a rarefaction wave develops. To evaluate the order of accuracy in respect to grid refinement, we run computation to $t=0.5/\pi$, and calculate the L_1 and L_∞ errors with different grid resolutions. A periodic boundary condition is imposed and our computation domain is set to be $[0,2]$. The numerical errors and convergence rate are shown in Table 2.

Table 2: Numerical errors and convergence rate for 1D Burgers equation at $t=1/(2\pi)$.

N	L_1 error	Order of Accuracy	L_∞ error	Order of Accuracy
40	1.11e-05		9.03e-05	
80	8.13e-07	3.86	7.37e-06	3.61
160	5.61e-08	3.86	5.33e-07	3.79
320	3.79e-09	3.89	3.61e-08	3.88
640	2.52e-10	3.91	2.35e-09	3.94

We see again that the MCV-WENO4 scheme uniformly converges up to 4th-order accuracy for this nonlinear test.

Example 4.5 (Test with shock)**.** This test for 1D inviscid Burgers equation includes both shock and rarefaction wave. The initial profile is given by

$$u(x,0)=\begin{cases}1, & 0.3\leqslant x\leqslant 0.75,\\ 0.5, & \text{otherwise.}\end{cases} \tag{4.9}$$

The numerical solutions at $t=0.2$ is displayed in Fig. 4. We can see that the numerical solution well resolves the shock wave without spurious oscillation, as well as the expansion wave without significant dissipation.

https://doi.org/10.4208/cicp.081214.250515s Published online by Cambridge University Press

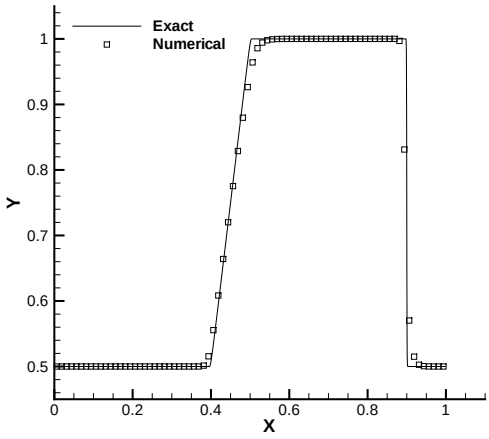


Fig. 4: Numerical results of Burgers equation with a shock and rarefaction at $t=0.2$ with 80 cells.

4.3 Buckley-Leverett equation

We show in this subsection the numerical solutions of the Buckley-Leverett equation,

$$u_t+\left(\frac{u^2}{u^2+(1-u)^2}\right)_x=0. \tag{4.10}$$

The upwinding scheme Eq. (4.8) is used as the approximate solver for the derivatives of the flux function at cell boundaries.

Example 4.6 (Two pulse interaction test)**.** Initially, we set the following conditions

$$u(x,0)=\begin{cases}1-20x, & 0\leqslant x\leqslant 0.05,\\ 0.5, & 0.25\leqslant x\leqslant 0.4,\\ 0, & \text{otherwise.}\end{cases} \tag{4.11}$$

The computation is carried out up to $t=0.5$ using 80 cells, and we show the results at $t=0.1$, $t=0.2$, $t=0.4$ and $t=0.5$ in Fig. 5. It is clear that the MCV-WENO4 scheme can reproduce the merging of two pulses well and recover good resolution for rarefaction wave.

4.4 1D Euler equations

Example 4.7 (Sod and Lax problems)**.** These two tests are the 1D shock tube problem proposed in [25,28]. For Sod's problem, the initial distribution is given by

$$(\rho_0,v_0,p_0)=\begin{cases}(1,0,1), & 0\leqslant x\leqslant 0.5,\\ (0.125,0,0.1), & \text{otherwise.}\end{cases} \tag{4.12}$$

https://doi.org/10.4208/cicp.081214.250515s Published online by Cambridge University Press

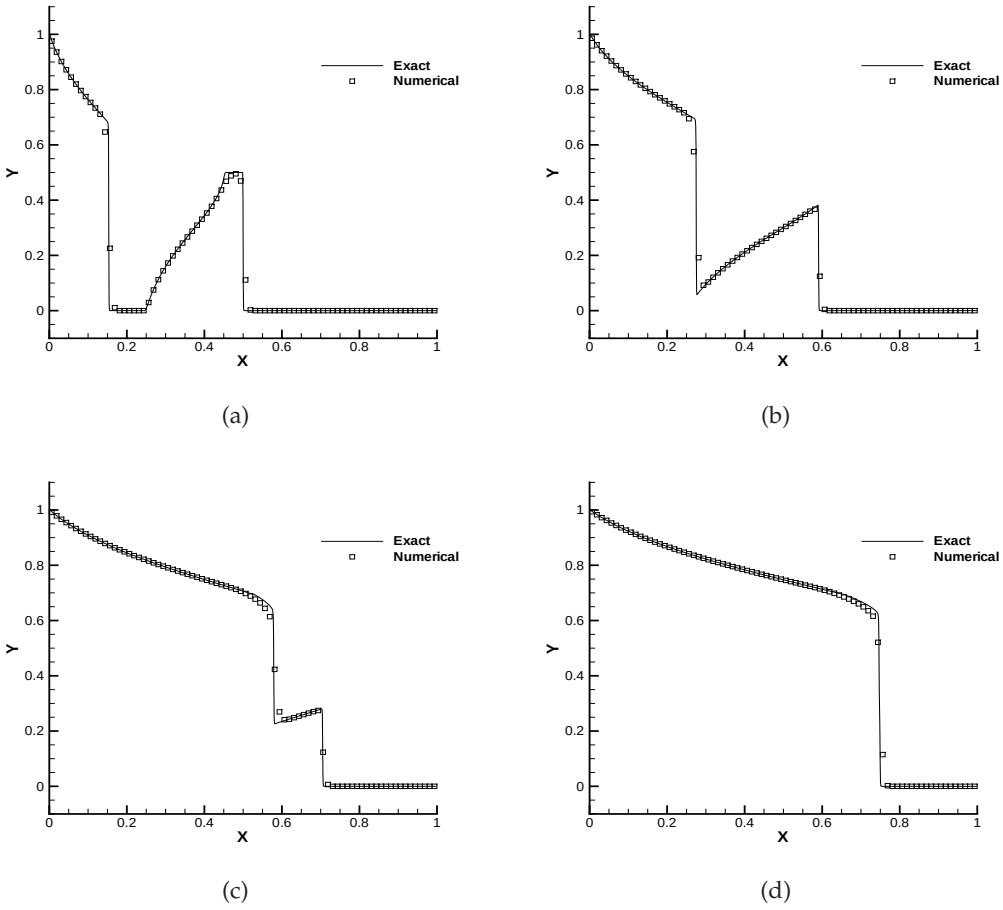


Fig. 5: Numerical results of 1D Buckley-Leverett equation at (a) $t=0.1$, (b) $t=0.2$, (c) $t=0.4$, (d) $t=0.5$ with 80 cells.

For Lax's problem, the initial profile is given by

$$(\rho_0,v_0,p_0)=\begin{cases}(0.445,0.698,3.528), & 0\leqslant x\leqslant 0.5,\\ (0.5,0,0.571), & \text{otherwise.}\end{cases} \tag{4.13}$$

We use a 100-cell mesh for both of these tests. In Sod's test, the computation is carried out up to $t=0.25$, while in Lax's problem we conduct the computation to $t=0.16$. The numerical results are shown in Figs. 6 and 7. In both of the two tests, an expansion wave, a contact discontinuity and a shock is generated. We can see that our results can suppress the oscillations near the shock and resolve both contact discontinuity and expansion wave with good accuracy.

https://doi.org/10.4208/cicp.081214.250515s Published online by Cambridge University Press

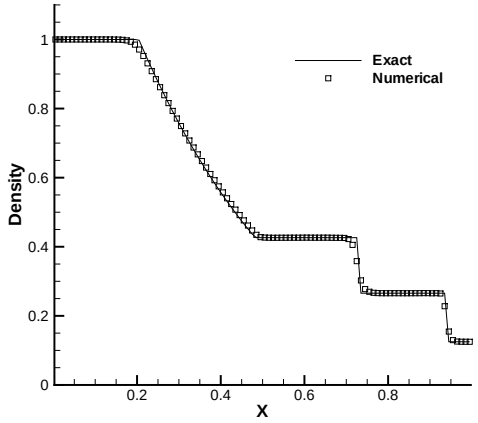


Fig. 6: Numerical results of Sod's problem at $t=0.25$ with 100 cells.

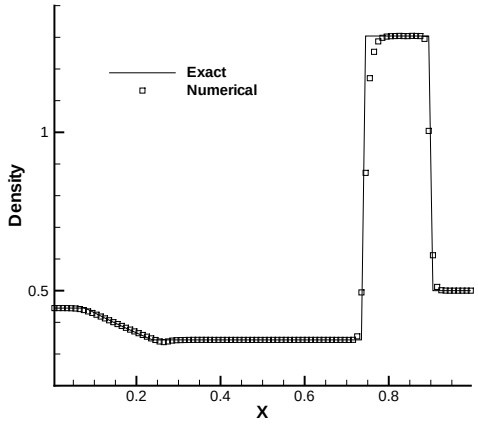


Fig. 7: Numerical results of Lax's problem at $t=0.16$ with 100 cells.

Example 4.8 (Symmetry expansion wave [32])**.** For this test problem, the initial condition is given by

$$(\rho_0,v_0,p_0)=\begin{cases}(1.0,-2.0,0.4), & 0\leqslant x\leqslant 0.5,\\ (1.0,2.0,0.4), & \text{otherwise.}\end{cases} \tag{4.14}$$

This test describes an isentropic process. Both density and pressure are uniform in the whole domain, while a divergent velocity field split the flow field with an initial velocity having opposite directions at the center of computational domain. Our computation is carried out up to $t=0.15$ with 200 cells over $[0,1]$. We show the numerical solutions of density, velocity, pressure and internal energy in Fig. 8. We find that the MCV-WENO4 scheme can accurately reproduce all the physical fields.

https://doi.org/10.4208/cicp.081214.250515s Published online by Cambridge University Press

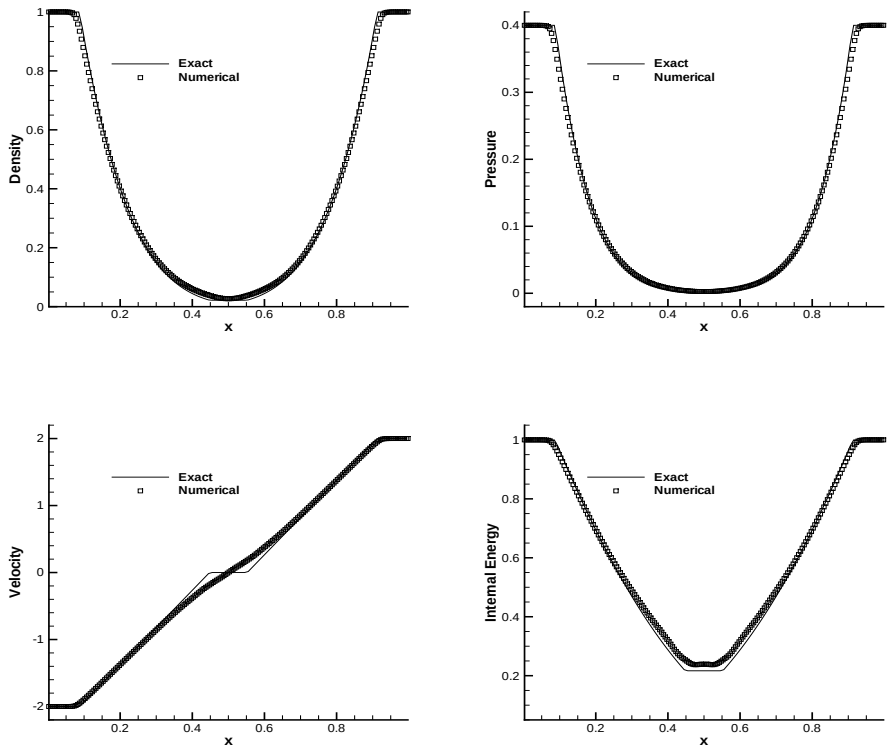


Fig. 8: Numerical results of symmetrical expansion problem at $t=0.15$ with 200 cells.

Example 4.9 (Shock-turbulence interaction)**.** This test problem is proposed in [27] to simulate a Mach 3 shock interacting with a density wave. The initial profile is given by

$$(\rho_0,v_0,p_0)=\begin{cases}(3.857143,2.629369,10.333333), & \text{when } x<0.1,\\ (1.0+0.2\sin(50x-25),0,1.0), & \text{when } x\geqslant 0.1.\end{cases} \tag{4.15}$$

A Mach 3 shock is initially located at $x=0.1$ and moves to the right. The initial density in the right part to the shock is generated by superimposing a sine-wave perturbation. The final results contain both the shock and smooth solutions. We perform the calculation until $t=0.18$ with 200 cells over $[0,1]$. The numerical solutions are shown in Fig. 9. The reference solution plotted by the solid line is computed by a fifth order WENO scheme of Jiang and Shu [15] with 2000 grid points. Our results show that there are no visible oscillations near the shock. Meanwhile, the density perturbation has been resolved accurately.

Example 4.10 (Two interacting blast waves)**.** This test problem was introduced by Wooward and Colella in [37]. Multiple interaction of strong shocks and rarefactions are

https://doi.org/10.4208/cicp.081214.250515s Published online by Cambridge University Press

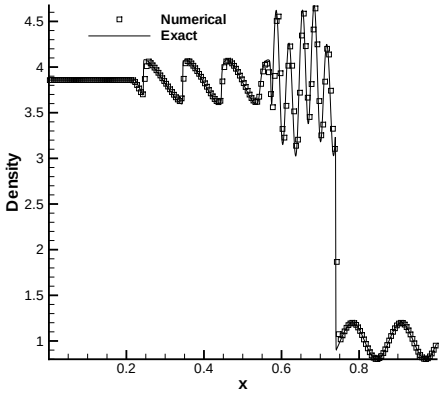


Fig. 9: Numerical results of shock-turbulence interaction at $t=0.18$ with 200 cells.

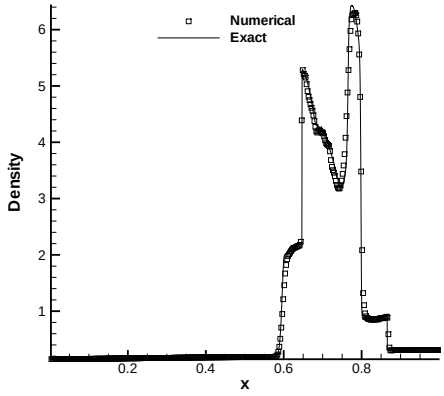


Fig. 10: Numerical results of two interacting blast waves at $t=0.038$ with 400 cells.

included in this test problem. The initial condition with only the pressure difference is given by

$$(\rho_0,v_0,p_0)=\begin{cases}(1,0,1000), & \text{if } 0\leqslant x\leqslant 0.1,\\ (1,0,0.01), & \text{if } 0.1<x<0.9,\\ (1,0,100), & \text{otherwise.}\end{cases} \tag{4.16}$$

The computation is conducted with 400 cells and reflective boundary condition. We give the numerical solutions of density ρ at $t=0.038$ in Fig. 10, where the reference solution is computed by the finite volume scheme with MUSCL reconstruction on a grid of 4000 cells. We can see that our numerical solution fits well with the exact solution.

Given the fact that only two local DOFs per cell is used in the present scheme, we may conclude that the numerical results of Examples 4.9 and 4.10 are among the best ever seen in the existing literature.

4.5 2D linear advection equation

In this subsection, we consider the 2D linear advection equation,

$$u_t+v_1u_x+v_2u_y=0, \tag{4.17}$$

where (v_1,v_2) are the velocity components in x and y directions. For 2D linear advection equation, all our computation is performed on uniform Cartesian grid.

Example 4.11 (Accuracy test)**.** The accuracy test for 2D linear advection equation is conducted by using the mesh refinement. The initial smooth profile is given by

$$u(x,y,0)=\sin(\pi(x+y)),\quad x\in[-1,1],\quad y\in[-1,1]. \tag{4.18}$$

https://doi.org/10.4208/cicp.081214.250515s Published online by Cambridge University Press

Table 3: Numerical errors and convergence rate for 2D advection equation, $t=2.0$.

$N_x\times N_y$	L_1 error	Order of Accuracy	L_∞ error	Order of Accuracy
10×10	1.55e-03		2.90e-03	
20×20	9.79e-05	3.98	1.54e-04	4.24
40×40	6.21e-06	3.98	9.77e-06	3.98
80×80	3.91e-07	3.99	6.15e-07	3.99

Here the velocity is set to be the constant value $(v_1,v_2)=(1,1)$. The computation is carried out up to $t=2.0$ (after one period), and the periodic boundary condition is specified for this problem. From Table 3, we can see that the expected order of accuracy can be achieved by MCV-WENO4 scheme.

Example 4.12 (Transport of complex profile)**.** In this test, the 2D complex initial profile is given by

$$u(x,y,0)=\begin{cases}\dfrac{1}{6}(G(r_1+\delta,\beta)+G(r_1-\delta,\beta)+4G(r_1,\beta)), & |r_1|\leqslant0.2,\\ 1, & |x|\leqslant0.2,\ -0.7\leqslant y\leqslant-0.3,\\ 1-|5r_2|, & |r_2|\leqslant0.2,\\ \dfrac{1}{6}(F(r_3+\delta,\alpha)+F(r_3-\delta,\alpha)+4F(r_3,\alpha)), & |r_3|\leqslant0.2,\\ 0, & \text{otherwise,}\end{cases}\tag{4.19}$$

where

$$r_1=\sqrt{(x+0.6)^2+y^2},\quad r_2=\sqrt{(x-0.6)^2+y^2},\quad r_3=\sqrt{x^2+(y-0.6)^2},$$

and $G(r,\beta)=\exp(-\beta r^2)$, $F(r,\alpha)=\sqrt{\max(1-\alpha^2r^2,0)}$. The coefficients are set to be $\delta=0.01$, $\alpha=5$ and $\beta=\log2/(36\delta^2)$. The rotational velocity field is defined by $(v_1,v_2)=(-2\pi y,2\pi x)$ and the computation domain is $[-1,1]\times[-1,1]$. Our computation is executed up to $t=1.0$ on two grids of 50×50 and 100×100 respectively. The numerical results are shown in Fig. 11. We can see that there are no visible oscillations near the jump discontinuities, and the numerical solution resolves all the structures adequately even on a grid of low resolution.

4.6 2D Euler equations

In this subsection, we solve the 2D Euler equations

$$\frac{\partial\mathbf{u}}{\partial t}+\frac{\partial\mathbf{f}(\mathbf{u})}{\partial x}+\frac{\partial\mathbf{g}(\mathbf{u})}{\partial y}=0,\tag{4.20}$$

https://doi.org/10.4208/cicp.081214.250515s Published online by Cambridge University Press

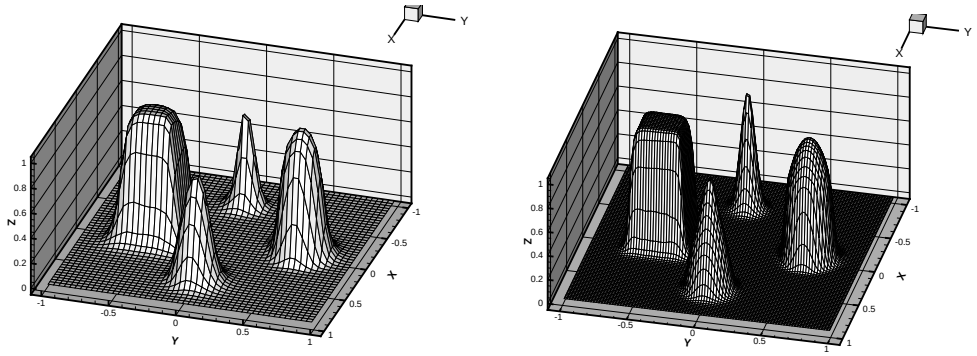


Fig. 11: Numerical results of 2D rotation test at $t=1.0$ on 50×50 (left) and 100×100 (right) grids.

where

$$\mathbf{u}=\begin{pmatrix}\rho\\ \rho u\\ \rho v\\ E\end{pmatrix},\quad \mathbf{f}(\mathbf{u})=\begin{pmatrix}\rho u\\ \rho u^2+p\\ \rho uv\\ u(E+p)\end{pmatrix},\quad \mathbf{g}(\mathbf{u})=\begin{pmatrix}\rho v\\ \rho uv\\ \rho v^2+p\\ v(E+p)\end{pmatrix}, \tag{4.21}$$

and (v_1,v_2) are the velocity components in x and y directions.

Example 4.13 (Accuracy test for 2D Euler equations)**.** To test the convergence rate of the MCV-WENO4 scheme, we use the following initial condition [20]

$$\begin{cases}\rho(x,y,0)=1+0.2\sin(\pi(x+y)),\\ u(x,y,0)=0.7,\\ v(x,y,0)=0.3,\\ p(x,y,0)=1.0,\end{cases}\qquad x\in[-1,1],\ y\in[-1,1]. \tag{4.22}$$

With the velocity and pressure fields specified uniformly over the whole computation domain, only the perturbation of density is transported. The convergence rate is evaluated via the grid refinement. The L_1 and L_∞ errors of density are shown in Table 4. Here the N_x and N_y are the mesh number in x direction and y direction. We can clearly see that the MCV-WENO4 scheme can achieve the convergence rate of 4th order for 2D Euler equations as expected.

Table 4: Numerical errors and convergence rate for density perturbation test of 2D Euler equations at $t=2.0$.

$N_x\times N_y$	L_1 error	Order of Accuracy	L_∞ error	Order of Accuracy
10×10	1.61e-04		3.00e-04	
20×20	1.04e-05	3.95	1.64e-05	4.20
40×40	6.66e-07	3.97	1.05e-06	3.97
80×80	4.20e-08	3.99	6.60e-08	3.99

https://doi.org/10.4208/cicp.081214.250515s Published online by Cambridge University Press

Example 4.14 (Isentropic vortex)**.** This test is a 2D vortex evolution problem [10, 47], which is used to examine the order of accuracy of a scheme for the 2D Euler equations (4.20) when solving flows of strong nonlinearity. In this test, an isentropic vortex is propagated by a mean flow defined by $(\rho_\infty,u_\infty,v_\infty,p_\infty)=(1,1,1,1)$. The perturbation is given as

$$(\delta u,\delta v)^T=\frac{\epsilon}{2\pi}\exp\left(\frac{1-r^2}{2}\right)(-y,x)^T,\quad \delta T=-\frac{(\gamma-1)\epsilon^2}{8\gamma\pi^2}\exp(1-r^2), \tag{4.23}$$

where $r^2=x^2+y^2$, $T=\frac{p}{\rho}$ is the temperature and $\epsilon=5.0$ the vortex strength. The solution of this test is the advection transport of the initial vortex along the diagonal direction. The computational domain is $[-5,5]\times[-5,5]$ with periodic boundary conditions. The L_1 and L_∞ errors of density at $t=10.0$ is shown in Table 5. We can see that convergence rate got from this test problem is not as uniform as the previous test. This phenomenon has also been observed for traditional WENO in [10]. It can be explained by the fact that in a coarse grid the smoothness indicator of WENO construction may incorrectly identify the smooth solutions with steep gradient as discontinuities. We can see from Table 5 that the our scheme tends to eventually converge to 4th order accuracy when the grid is sufficiently fine.

Table 5: Numerical errors and convergence rate for isentropic vortex of 2D Euler equations at $t=10.0$.

$N_x\times N_y$	L_1 error	Order of Accuracy	L_∞ error	Order of Accuracy
20×20	7.55e-03		9.93e-02	
40×40	5.57e-04	3.76	5.57e-03	4.15
80×80	1.67e-04	1.75	2.80e-03	9.95
160×160	2.02e-06	6.36	6.09e-04	2.20
320×320	4.48e-10	5.50	3.99e-06	7.25

Also, to visually illustrate the convergence rate of the numerical solution, we compute this test on a computation area $[-5,5]\times[-5,5]$ up to $t=10.0$ and $t=100.0$ with the periodic boundary condition. We use a mesh of 32×32. The density distribution of numerical solutions on $y=0$ cross section is plotted in Fig. 12. We can see that the numerical solutions maintain visually identical to the analytical solutions at $t=10.0$, while at $t=100.0$ there is a slight accumulation of numerical dissipation which is acceptable for such a long term computation on a low resolution grid.

Example 4.15 (2D explosive test)**.** This test, as shown in [32], is an axi-symmetric two-dimensional explosion problem. Initially, the region inside a circle of radius $R=0.4$ is set with high pressure and density while the region out of the circle is of low pressure and density as,

$$(\rho,u,v,p)=\begin{cases}(1.0,0.0,0.0,1.0), & \text{if } r\leqslant R,\\ (0.125,0.0,0.0,0.1), & \text{if } r>R,\end{cases} \tag{4.24}$$

https://doi.org/10.4208/cicp.081214.250515s Published online by Cambridge University Press

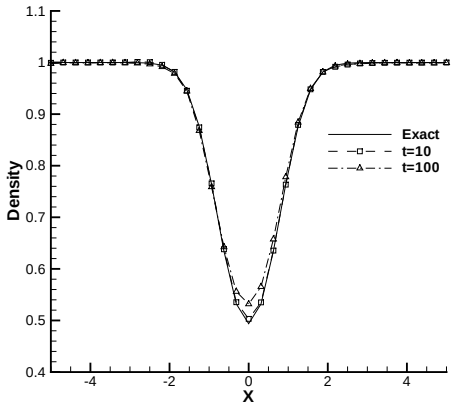


Fig. 12: The density distribution of numerical solutions on $y=0$ cross section at $t=10.0$ and $t=100.0$ with 32×32 cells.

where $r=\sqrt{x^2+y^2}$ is the radius. So the fluid inside the circle will spread out to form a shock, a contact discontinuity and a rarefaction wave of cylindrical symmetry.

Our computation is run up to $t=0.25$ on a 200×200 grid. We show the bird's eye view of density and pressure in Fig. 13. It is observed that the MCV-WENO4 scheme can well reproduce all the shock wave, contact discontinuity and rarefaction fan with perfect symmetry.

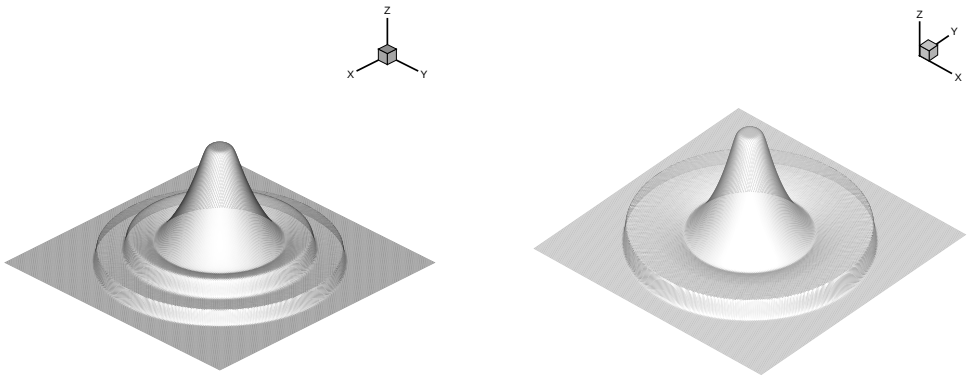


Fig. 13: Numerical results of 2D explosive test at $t=0.25$ with 200×200 cells. Displayed are density (left) and pressure (right).

Example 4.16 (Double Mach reflection)**.** This is a widely used test problem [37] to evaluate the ability of a scheme to capture both shock and vortex structures.

As detailed in [37], the computation domain is set to be $[0,3.2]\times[0,1]$. A right-moving Mach 10 shock positioned at $(\frac{1}{6},0)$ initially makes a 60° angle to the bottom boundary where a reflective boundary is imposed from $x=\frac{1}{6}$ to $x=3.2$. In the region of $x\in[0,\frac{1}{6}]$

https://doi.org/10.4208/cicp.081214.250515s Published online by Cambridge University Press

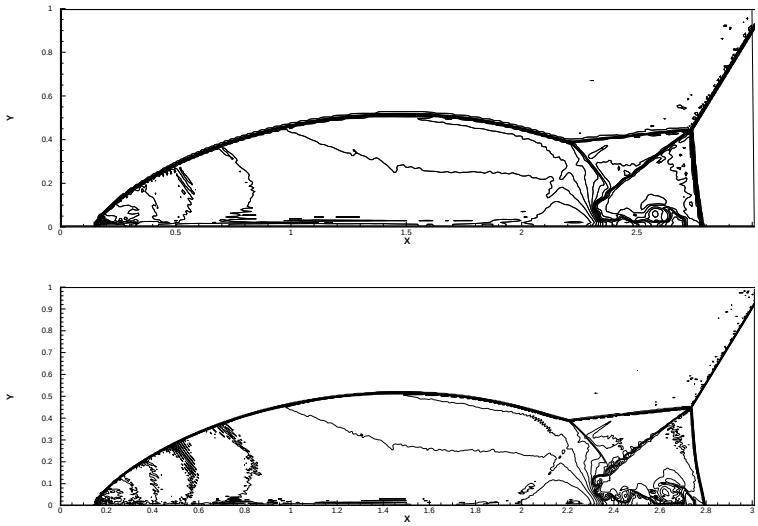


Fig. 14: Numerical results of double Mach reflection at $t=0.2$ with 120×384 cells (top), 250×800 cells (bottom).

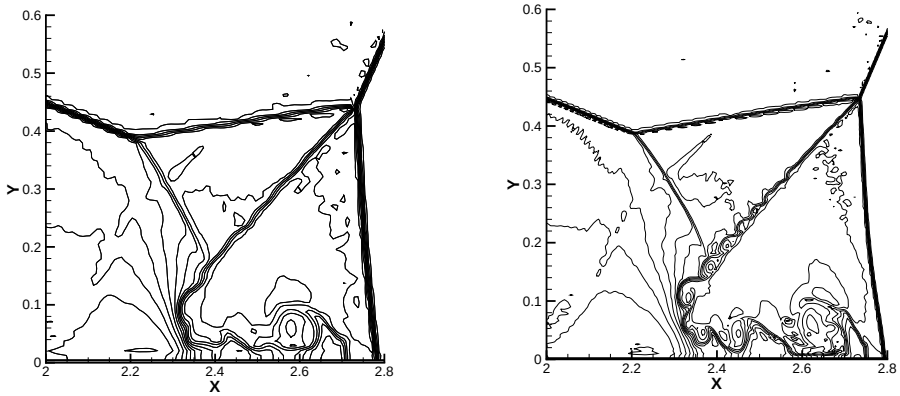


Fig. 15: Numerical results of double Mach reflection at $t=0.2$ with 120×384 cells (left), 250×800 cells (right).

on the bottom boundary, as well as the left boundary, we impose the exact post shock condition. At the right boundary we set all the gradients to be zero. At the top boundary, the values of the flow are set to describe the exact motion of right moving Mach 10 shock. We carried out the computation up to $t=0.2$. In Fig. 14, we give the numerical solutions calculated respectively by 120×384 cells and 250×800 cells. We see that with the refinement of the mesh resolution, the vortex structure between two strong shocks can be resolved adequately. Also, we show the "blown-up" portion around the double Mach region in Fig. 15. It is found that our scheme can clearly recover the structure of the vortex with a reasonable high resolution.

https://doi.org/10.4208/cicp.081214.250515s Published online by Cambridge University Press

Example 4.17 (Shock-vortex interaction in two dimensions)**.** This test which was originally presented in [15] describes the interaction between a Mach 1.1 stationary shock and an isentropic vortex. The computational domain is set to be $[0,2]\times[0,1]$. Initially, a stationary shock is defined along the line $x=0.5$, with next jump conditions

$$(\rho,u,v,p)=\begin{cases}(1.0,1.1\sqrt{\gamma},0.0,1.0), & \text{if } x\leqslant 0.5,\\ (1.169082121,0.940909094\sqrt{\gamma},0.0,1.244999994), & \text{if } x>0.5.\end{cases} \tag{4.25}$$

Given the left side state, the right state of stationary shock is calculated from Rankine-Hugoniot condition.

The vortex is located at the center of the super-sonic area $(x_c,y_c)=(0.25,0.5)$. The initial structure of the vortex is generated from the following perturbation,

$$(\delta u,\delta v)^T=\epsilon\tau e^{\alpha(1-\tau^2)}(\sin(\theta),-\cos(\theta))^T,\quad \delta T=-\frac{(\gamma-1)\epsilon^2}{4\alpha\gamma}e^{2\alpha(1-\tau^2)},\quad \delta S=0, \tag{4.26}$$

where $\tau=r/r_c$, $r=\sqrt{(x-x_c)^2+(y-y_c)^2}$ and $r_c=0.05$ is the critical radius of the vortex. $\epsilon=0.3$ is the strength of the vortex, and $\alpha=0.204$ is related to the decay rate of the vortex. θ represents the angle between the angular velocity and the horizontal axis. The top and bottom boundaries are set to be reflective walls.

We compute this test problem on a grid of 50×100 in order to compare with the results in [15]. We show the pressure contour at $t=0.05$, 0.2, 0.35 and 0.6 in Fig. 16. For $t=0.05$, 0.2 and 0.35, the reflective wall does not significantly affect the flow field, while at $t=0.6$, the bifurcation of shock is reflected by the top and bottom walls. It can be observed that our results can well resolve the interaction between the vortex and shock with competitive quality in comparison with the previous works.

5 Conclusion

In this paper, we have presented and tested a new WENO-type limiter for the 3-point MCV scheme under the MMC-FR framework. The basic idea is to reconstruct the first order derivative at the cell center of the MCV-SC scheme using the WENO methodology.

Compared with other existing methods, the present scheme has at least following advantages. 1) The WENO reconstruction is based on the sub-grid solution structures from the nodal values at the solution points within the target cell and its immediate neighbors. The stencil for reconstruction is minimized. Thus, the scheme is better suited for the local high-order reconstruction schemes where sub-grid information is available. 2) The present scheme has much less numerical dissipation to the smooth solution, and thus doesn't use the ad hoc TVB criterion (or so-called "trouble cell indicator") that is needed in nearly all existing schemes. 3) The present scheme is algorithmically simple and computationally efficient.

https://doi.org/10.4208/cicp.081214.250515s Published online by Cambridge University Press

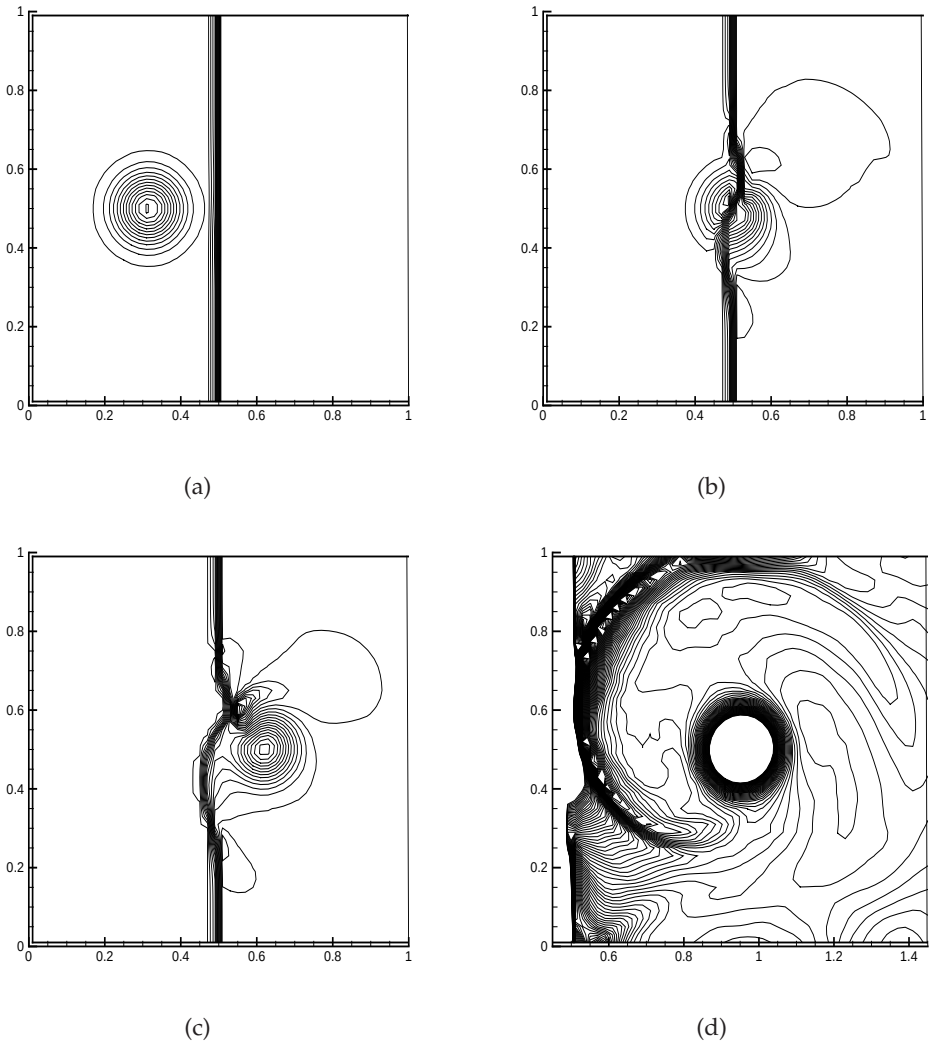


Fig. 16: Numerical results of shock-vortex interaction problem at (a) $t=0.05$, (b) $t=0.2$, (c) $t=0.35$ and (d) $t=0.6$ on a 50×100 mesh. The number of contours is 30 for (a)-(c) and 90 for (d) respectively.

The numerical results for the widely used benchmark tests show that our scheme can get the 4th-order uniform convergence rate as expected and high quality solutions for both discontinuities and smooth profiles.

Acknowledgments

This work is supported in part by JSPS KAKENHI (24560187, 15H03916).

https://doi.org/10.4208/cicp.081214.250515s Published online by Cambridge University Press

References

[1] R. Borges, M. Carmona, B. Costa and W.S. Don, An improved weighted essentially non-oscillatory scheme for hyperbolic conservation laws, J. Comput. Phys., 227 (2008), 3191-3211.
[2] C.G. Chen, X.L. Li, X.S. Shen and F. Xiao, Global shallow water models based on multi-moment constrained finite volume method and three quasi-uniform spherical grids, J. Comp. Phys. 271(2014), 191-223.
[3] C.G.Chen and F.Xiao, Shallow water model on cubed-sphere by multi-moment finite volume method, J. Comput. Phys. 227(2008), 5019-5044.
[4] B. Cockburn and C.W. Shu, TVB Runge-Kutta local projection discontinuous Galerkin finite element method for conservation laws II: General framework, Math. Comput., 52 (1989), 411-435.
[5] B. Cockburn, S.Y. Lin and C.W. Shu, TVB Runge-Kutta local projection discontinuous Galerkin finite element method for conservation laws III: One-dimensional systems, J. Comput. Phys., 84 (1989), 90-113.
[6] B. Cockburn, S. Hou and C.W. Shu, TVB Runge-Kutta local projection discontinuous Galerkin finite element method for conservation laws IV: The multidimensional case, Math. Comput., 54 (1990), 545-581.
[7] J. Du, C.W. Shu and M.P. Zhang, A simple weighted essentially non-oscillatory limiter for the correction procedure via reconstruction (CPR) framework, Applied Numerical Mathematics, to appear (2014).
[8] A.K. Henrick, T.D. Aslam and J.M. Powers, Mapped weighted essentially nonoscillatory schemes: achieving optimal order near critical points, J. Comput. Phys., 207 (2005), 542-567.
[9] J.S. Hesthaven and T. Warburton, Nodal discontinuous Galerkin methods: Algorithms, analysis and applications, Springer, 2008.
[10] C.Q. Hu and C.W. Shu, Weighted Essentially Non-oscillatory Schemes on Triangular Meshes, J. Comput. Phys., 150 (1999), 97-127.
[11] C.S. Huang, F. Xiao and T. Arbogast, Fifth Order Multi-moment WENO Schemes for Hyperbolic Conservation Laws, Journal of Scientific Computing, in press (2014), DOI 10.1007/s10915-014-9940-z.
[12] H. T. Huynh, A flux reconstruction approach to high-order schemes including discontinuous Galerkin methods, AIAA Paper, 2007-4079 (2007).
[13] S. Ii and F. Xiao, CIP/multi-moment finite volume method for Euler equations, a semi-Lagrangian characteristic formulation, J. Comput. Phys., 222(2007), 849-871.
[14] S. Ii and F. Xiao, High order multi-moment constrained finite volume method. Part I: Basic formulation, J. Comput. Phys., 228(2009), 3669-3707.
[15] G.S. Jiang and C.W. Shu, Efficient implementation of weighted ENO schemes, J. Comput. Phys., 126 (1996), 202-228.
[16] D.A. Kopriva and J.H. Kolias, A conservative staggered-grid Chebyshev multidomain method for compressible flows, J. Comput. Phys., 125(1996), 244-261.
[17] X.L. Li, C.G. Chen, X.S. Shen and F. Xiao, A Multi-moment Constrained Finite-Volume Model for Nonhydrostatic Atmospheric Dynamics, Mon. Wea. Rev., 141(2013), 1216-1240.
[18] X.D. Liu, S. Osher and T. Chan, Weighted essentially non-oscillatory scheme, J. Comput. Phys., 115 (1994), 200-212.
[19] A. T. Patera, A spectral element methd for fluid dynamics: Laminar flow in a channel expansion, J. Comput. Phys., 54(1984), 468-488.
[20] J.X. Qiu and C.W. Shu, Hermite WENO schemes and their application as limiters for Runge-

https://doi.org/10.4208/cicp.081214.250515s Published online by Cambridge University Press

Kutta discontinuous Galerkin method: one-dimensional case, J. Comput. Phys., 193(2004), 115-135.
[21] J.X. Qiu and C.W. Shu, Runge-Kutta Discontinuous Galerkin Method Using WENO Limiters, SIAM J. Sci. Comput., 26 (2005), 907-929.
[22] P.L. Roe, Approximate Riemann solvers, parameter vectors, and difference schemes, J. Comput. Phys., 43(1981), 357-372.
[23] Y.Q. Shen, G.C. Zha, Improvement of weighted essentially non-oscillatory schemes near discontinuities, 19th AIAA Computational Fluid Dynamics, 22 - 25, June 2009, San Antonio, Texas, AIAA 2009-3655 (2009).
[24] Y.Q. Shen, G.C. Zha, Improvement of weighted essentially non-oscillatory schemes near discontinuities, Computers & Fluids, 96 (2014), 1-9.
[25] G.A. Sod, A survey of several finite difference methods for systems of nonlinear hyperbolic conservation laws, J. Comput. Phys., 27 (1978), 1-31.
[26] C.W. Shu, High Order Weighted Essentially Nonoscillatory Schemes for Convection Dominated Problems, SIAM Review, 51 (2009), 82-126.
[27] C.W. Shu and S. Osher, Efficient implementation of essentially non-oscillatory shock-capturing schemes, J. Comput. Phys., 77 (1988), 439-471.
[28] C.W. Shu and O. Osher, Efficient implementation of essentially non-oscillatory shock capturing schemes, II, J. Comput. Phys., 83 (1989), 32-78.
[29] R. Spiteri and S.J. Ruuth, A new class of optimal high-order strong-stability-preserving time discretization methods, SIAM J. Numer. Anal., 40 (2002), 469-491.
[30] Y. Sun, Z.J. Wang and Y. Liu, High-order multidomain spectral difference method for the Navier-Stokes equations on unstructured hexahedral grids, Comm. in Comput. Phys., 2 (2007), 310-333.
[31] V.A. Titarev and E.F. Toro, ADER: arbitrary high order Godunov approach, J. Sci. Comput., 17 (2002), 609-618.
[32] E.F. Toro, Riemann solvers and numerical methods for fluid dynamics: a practical introduction. Third edition, Springer-Verlag, Berlin, 2009.
[33] E.F. Toro and V.A. Titarev, Derivative Riemann solvers for systems of conservation laws and ADER methods, J. Comput. Phys., 212 (2006), 150-165.
[34] Z.J. Wang, Spectral (finite) volume method for conservation laws on unstructured grids: basic formulation, J. Comput. Phys., 178 (2002), 210-251.
[35] Z.J. Wang, Y. Liu, Spectral (finite) volume method for conservation laws on unstructured grids II: extension to two-dimensional scalar equation, J. Comput. Phys., 179 (2002), 665-697.
[36] Z.J. Wang and H.Y. Gao, A unifying lifting collocation penalty formulation including the discontinuous Galerkin, spectral volume/difference methods for conservation laws on mixed grids, J. Comput. Phys., 228 (2009), 8161-8186.
[37] P. Woodward and P. Colella, The numerical simulation of two-dimensional fluid flow with strong shocks, J. Comput. Phys., 54 (2009), 115–173.
[38] F. Xiao, S. Ii, C. G. Chen and X.L. Li, A note on the general multi-moment constrained flux reconstruction formulation for high order schemes, Appl. Math. Modelling, 37(2013), 5092-5108.
[39] F.Xiao, T.Yabe and T.Ito, Constructing Oscillation Preventing Scheme for Advection Equation by Rational Function, Computer Physics Communications, 93 (1996), 1-12.
[40] F.Xiao, T.Yabe, G.Nizam and T.Ito, Constructing a multi-dimensional oscillation preventing scheme for the advection equation by a rational function, Computer Physics Communica-

https://doi.org/10.4208/cicp.081214.250515s Published online by Cambridge University Press

tions, 94 (1996), 103-118.
[41] F.Xiao and T.Yabe, Completely conservative and oscillationless semi-Lagrangian schemes for advection transportation, J. Comput. Phys., 170(2001), 498-522.
[42] F.Xiao, T.Yabe, X.D.Peng and H.Kobayashi, Conservative and oscillation-less atmospheric transport schemes based on rational functions, J. Geophys. Res. 107(2002), D22, ACL2-1-ACL2-11. Doi: 10.1029/2001JD001532.
[43] B. Xie, S. Ii, A. Ikebata and F. Xiao, A multi-moment finite volume method for incompressible Navier-Stokes equations on unstructured grids: volume-average/point-value formulation, J. Comput. Phys., 277 (2014), 138-162.
[44] B. Xie and F. Xiao, Two and three dimensional multi-moment finite volume solver for incompressible Navier-Stokes equations on unstructured grids with arbitrary quadrilateral and hexahedral elements, Computers & Fluids, 104(2014), 40-54.
[45] T.Yabe and T.Aoki, A universal solver for hyperbolic equations by cubic-polynomial interpolation I. One-dimensional solver, Computer Physics Communications, 66 (1991), 219-232.
[46] T.Yabe, F.Xiao and T.Utsumi, The constrained interpolation profile method for multiphase analysis, J. Comput. Phys., 169(2001), 556-593.
[47] H. Yee, N. Sandham, and M. Djomehri, Low-dissipative high-order shock-capturing methods using characteristic-based filters, J. Comput. Phys., 150 (1999), 199-238.
[48] X. Zhong and C.W. Shu, A simple weighted essentially nonoscillatory limiter for Runge-Kutta discontinuous Galerkin methods, J. Comput. Phys., 232(2013), 397-415.

https://doi.org/10.4208/cicp.081214.250515s Published online by Cambridge University Press